

Monolayer fullerene networks as photocatalysts for overall water splitting

Bo Peng^{1,*}

¹*Theory of Condensed Matter Group, Cavendish Laboratory, University of Cambridge,
J. J. Thomson Avenue, Cambridge CB3 0HE, United Kingdom*

(Dated: August 2, 2022)

Photocatalytic water splitting can produce hydrogen in an environmentally friendly way and provide alternative energy sources to reduce global carbon emissions. Recently, monolayer fullerene networks have been successfully synthesized, offering new material candidates for photocatalysis because of their large surface area with abundant active sites, feasibility to be combined with other 2D materials to form heterojunctions, and the C₆₀ cages for potential hydrogen storage. However, efficient photocatalysts need a combination of a suitable band gap and appropriate positions of the band edges. In this study, I employ semilocal density functional theory and hybrid functional calculations to investigate the electronic structures of monolayer fullerene networks. I find that only the unscreened hybrid functional, in combine with time-dependent Hartree-Fock calculations to include the exciton binding energy, can reproduce the experimentally obtained optical band gap of monolayer C₆₀. All the phases of monolayer fullerene networks have suitable band gaps with appropriate band edges for overall water splitting. In addition, the optical properties of monolayer C₆₀ are studied, and different phases of fullerene networks exhibit distinct absorption and recombination behavior, providing unique advantages either as an electron acceptor or as an electron donor in photocatalysis.

The energy consumption of fossil fuels is the main source of global carbon emissions¹. As an alternative, hydrogen can be burnt in the presence of oxygen and produce only water, supporting mitigation of CO₂ emissions. Photocatalysis can decompose water into hydrogen and oxygen using light, providing a low-cost approach for the green production of hydrogen. Photocatalytic water splitting has been extensively studied since the discovery of electrochemical photolysis of water in TiO₂ in 1972²⁻¹⁰. However, due to the wide band gap of 3.0–3.2 eV in TiO₂, only the ultraviolet part of the solar spectrum can be harnessed. To maximize the photocatalytic efficiency, a water-splitting material need to (i) absorb the light effectively to generate enough electron-hole pairs; (ii) separate the generated carriers on the surface; and (iii) overcome the potential barrier of the reaction. For (i) and (iii), a compromise of the band gap is needed to harness the photon energy effectively while fulfilling the requirements of the band edges to facilitate the redox reaction of water. As a result, an optimal band gap around 2 eV is required, and the band edges must span the redox potential¹¹⁻¹³. For (ii), a type-II band alignment can spontaneously separate the electrons and holes. Based on these requirements, a variety of candidate materials have been proposed for efficient water splitting¹⁴⁻²¹. Among all the candidates, carbon nanomaterials exhibit high physical stability and rich redox chemistry^{22,23}. In particular, fullerene, the cage structure of C₆₀²⁴, displays high quantum efficiency in photocatalytic reactions because of their large surface area, abundant micropores, increased surface active sites and efficient electron transport properties²⁵⁻²⁸. In photocatalysis, C₆₀ can enhance the photocatalytic activity via different mechanisms: it can work as an electron acceptor owing to rapid carrier separation^{27,29-31}, or as an energy transfer mediator³², or as an electron donor due to high photosensitivity³³.

In addition, for composite materials, the introduction of fullerene results in better crystallization by reducing the defects²⁸, and can also improve the stability of the composites^{34,35}, which further enhance the photocatalytic efficiency. Most interestingly, C₆₀ itself is a promising hydrogen storage material^{36,37}, and photocatalytic water splitting using fullerene provides a convenient approach to produce and store hydrogen at the same time.

Recently, a 2D material composed of covalently bonded fullerene network structures has been synthesized, with two configurations obtained: a quasi-tetragonal phase (qTP) and a quasi-hexagonal phase (qHP)³⁸. The various structural phases of monolayer fullerene networks can be combined with other 2D materials to form type-II van der Waals heterostructures³⁹⁻⁴¹, which can efficiently separate carriers between individual layers. In addition, the band alignment in 2D heterostructures can be further controlled by external strain because of the mechanical flexibility of 2D materials⁴²⁻⁴⁴. Compared to heterostructures using C₆₀ molecules⁴⁵, heterostructures using monolayer polymetric fullerene has a smooth microscopic surface with uniform periodic C₆₀ networks, which provides high crystallinity and consequently increases the photocatalytic activity. Compared to other 2D materials⁴⁶⁻⁵⁷, monolayer C₆₀ has larger surface area with more active sites due to the quasi-0D network structures of C₆₀ cages. Additionally, monolayer C₆₀ exhibits good thermodynamic stability and high carrier mobility³⁸. All these physical/chemical properties render monolayer fullerene networks a promising candidate for photocatalytic water splitting. However, all theoretical calculations underestimate the band gap of monolayer C₆₀ by at least 10%^{42,43,58}, and a correct description of the band structures is the prerequisite for exploring the band edge positions for water splitting or the optical absorption for photocatalysis.

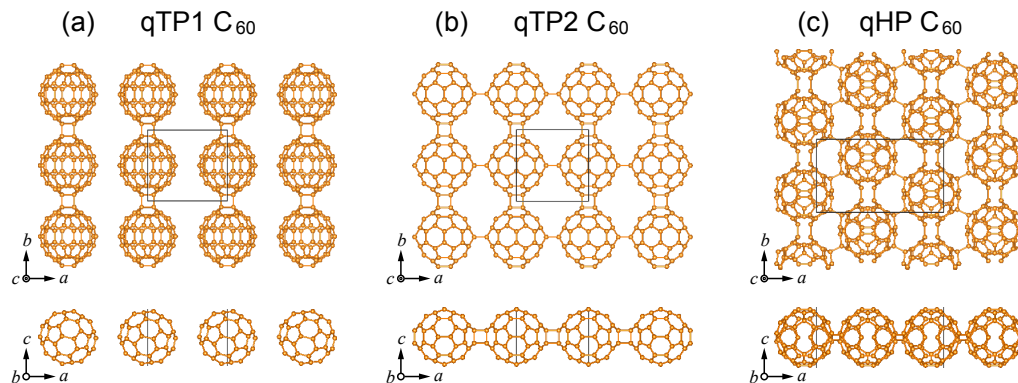


FIG. 1. Crystal structures of monolayer (a) qTP1, (b) qTP2 and (c) qHP C_{60} from top and side views.

In this paper, the electronic structures of monolayer qTP and qHP fullerene networks are investigated using semilocal density functional theory (DFT) and hybrid functional calculations. By examining the band gap and exciton binding energy, I find that the electronic structures and optical properties of monolayer C_{60} can only be describe correctly by unscreened hybrid functional. The band gaps of monolayer fullerene are around 2.12 – 2.31 eV, with the band edge positions ideally suitable for overall water splitting. The carrier recombination in qTP C_{60} is suppressed by weak optical transition, leading to efficient carrier separation as an electron acceptor. On the other hand, the strong optical absorption in qHP C_{60} can provide a large amount of electrons for hydrogen evolution, making it promising as an electron donor. These results indicate that monolayer fullerene networks are promising as efficient overall water splitting photocatalysts.

All crystal structures of monolayer fullerene networks are optimized using the PBEsol functional⁵⁹ as implemented in VASP^{60,61}. A plane-wave cutoff of 800 eV and a 5×5 (3×5) \mathbf{k} -mesh are used for qTP (qHP) C_{60} during the structural relaxation, with an energy convergence criterion of 10^{-6} eV and a force convergence criterion of 10^{-2} eV/Å. To mimic the 2D monolayers with 3D periodic boundary conditions, an interlayer vacuum spacing larger than 17 Å is used to eliminate interactions between adjacent unit cells along the c direction.

The crystal structures of monolayer fullerene networks are present in Fig. 1. After geometry optimization, two quasi-tetragonal phases are obtained. One phase, denoted as qTP1, crystallizes in space group $P2/m$ (No. 10) with lattice parameters $a = 10.175$ Å and $b = 9.059$ Å, in which each C_{60} is linked by two neighboring C_{60} cages through two $[2+2]$ cycloaddition bonds along the b direction, forming 1D chains of C_{60} cluster cages. The shortest interchain distance between the nearest carbon atoms is 3.065 Å along the a direction, which is much longer than the C–C single bonds. The interchain distance is shortened merely by 0.167 Å when including the van der Waals interactions⁶², therefore the van der Waal interactions are negligible in qTP1 C_{60} . The space group

of the other quasi-tetragonal phase, demoted as qTP2, is $Pmmm$ (No. 47), with lattice parameters $a = 9.097$ Å and $b = 9.001$ Å. Similar to qTP1 C_{60} , the in-plane $[2+2]$ cycloaddition bonds connect neighboring C_{60} cages along the b direction in qTP2 C_{60} . The difference between qTP1 and qTP2 C_{60} is along the a direction: no bond is formed between neighboring C_{60} chains in qTP1 fullerene along the a direction, whereas each C_{60} cage of qTP2 fullerene connects two neighboring cages along that direction through two out-of-plane $[2+2]$ cycloaddition bonds, as demonstrated in Fig. 1(b). Monolayer qHP C_{60} has a space group of Pc (No. 7) with lattice parameters $a = 15.848$ Å and $b = 9.131$ Å, where each C_{60} is connected to six neighboring C_{60} cages with four C–C single bonds along the diagonal lines of the rectangular unit cell and two $[2+2]$ cycloaddition bonds along the b direction. The calculated lattice constants agree well with previous calculations⁴².

From these crystal structures, the electronic structures of qTP1, qTP2 and qHP C_{60} are predicted using the PBEsol functional⁵⁹ and the screened hybrid functional HSEsol⁶⁴. The band structures of qTP1 C_{60} are shown in Fig. 2(a). The obtained PBEsol and HSEsol band gaps are 1.09 and 1.65 eV respectively, with the valence band maximum (VBM) at the Y high-symmetry point and the conduction band minimum (CBM) at X. As both PBEsol and HSEsol functionals tend to overestimate the screening effects in low-dimensional systems and consequently underestimate their band gap^{65–67}, the band gap is also evaluated by using unscreened hybrid functional in which the Hartree-Fock and PBEsol exchange energies are mixed in a 1:3 ratio along with the full PBEsol correlation energy (denoted as PBEsol0)^{68–70}. With the screening parameter decreases to 0 Å⁻¹, i.e. the long-range Hartree-Fock exchange is unscreened, the band gap further increases to 2.31 eV, as listed in Table I.

To visualize the band edges, the partial charge density at specific \mathbf{k} -points and electronic bands is shown in Fig. 2(d). The highest valence band is flat along Γ –X, and as expected, the corresponding charge density of VB1 is isolated within separated C_{60} cages. Similarly, the top valence states and lowest conduction states at Y, denoted

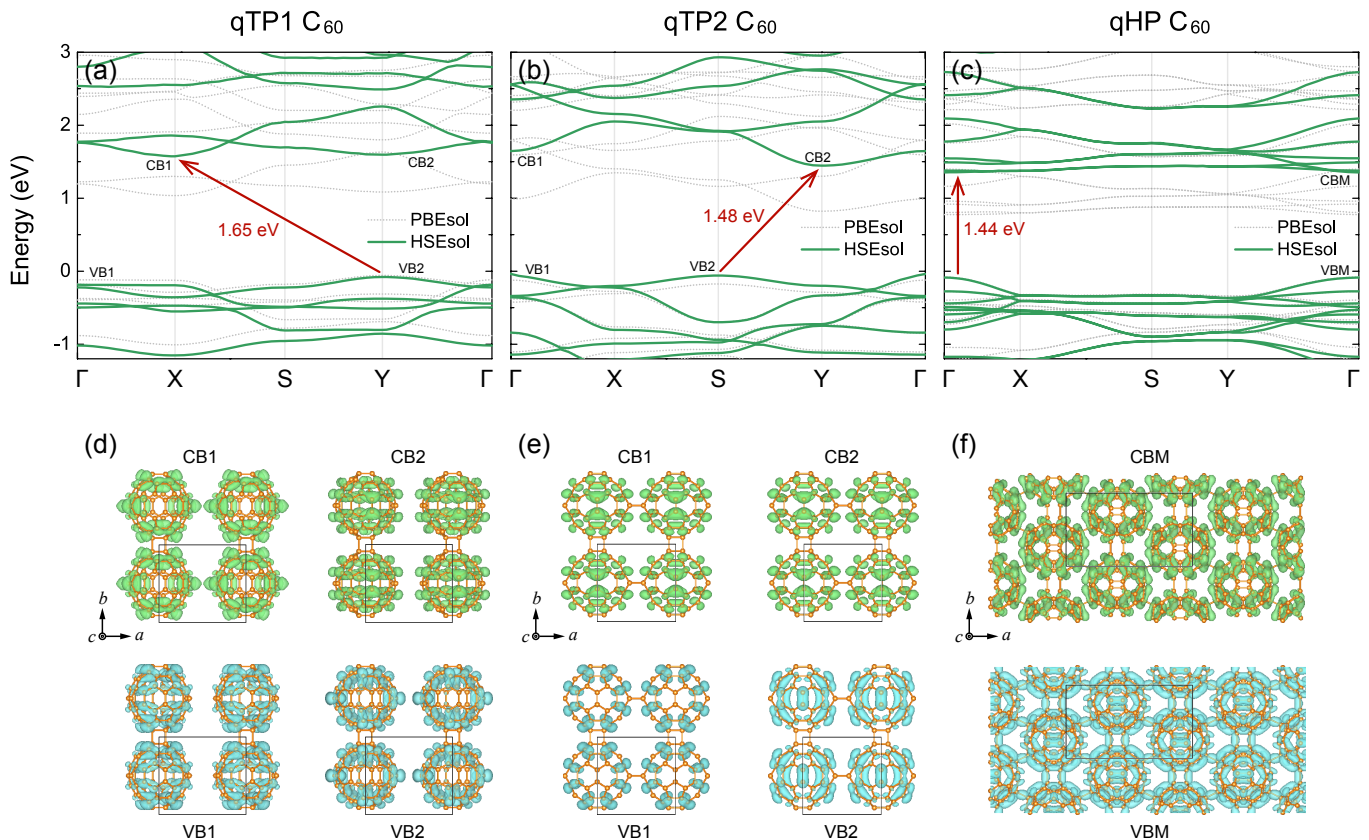


FIG. 2. Electronic structures of (a) qTP1, (b) qTP2, and (c) qHP C_{60} calculated with PBEsol functional and HSEsol hybrid functional, as well as their corresponding partial charge density of the top valence states and the lowest conduction states in (d)-(f). The default isosurface level is used, as implemented in VESTA⁶³.

TABLE I. Calculated band gaps (eV) of qTP1, qTP2 and qHP C_{60} using PBEsol, HSEsol and unscreened hybrid functional PBEsol0 with their corresponding screening parameter μ (\AA^{-1}).

	PBEsol HSEsol PBEsol0		
	μ	∞	0
qTP1	1.09	1.65	2.31
qTP2	0.94	1.48	2.18
qHP	0.86	1.44	2.12

as VB2 and CB2 respectively, are centered around each single C_{60} cage, and such molecular-like character is consistent with their flat bands. Compared to VB1, VB2 and CB2, the lowest conduction band at X (CB1) is more dispersive and its charge density is more diffuse along the a direction.

For qTP2 C_{60} , the PBEsol functional predicts an indirect band gap of 0.94 eV with the VBM at Γ and the CBM at Y, while the HSEsol hybrid functional yields an indirect gap of 1.48 eV with the VBM at S and the CBM at Y. As shown in Fig. 2(b), the band structures of qTP2 C_{60} show distinct difference from qTP1 C_{60} ,

despite that their lattice parameters are similar. In addition, the charge density of qTP2 C_{60} changes significantly compared to that of qTP1 C_{60} . Because the space group of qTP2 C_{60} ($Pmmm$) has more symmetry operations than that of qTP1 C_{60} ($P2/m$), their partial charge density in Fig. 2(e) is more symmetric than that of qTP1 C_{60} .

Figure 2(c) depicts the PBEsol and HSEsol band structures of monolayer qHP C_{60} . Monolayer qHP C_{60} possesses a direct band gap at Γ . The CBM of monolayer qHP C_{60} exhibits flat-band features, and its charge density is molecular-like, as shown in Fig. 2(f). On the other hand, the charge of the more dispersive VBM is distributed in the entire Brillouin zone, connecting neighboring C_{60} cages via both the C–C single bonds and the [2+2] cycloaddition bonds. Therefore, holes are expected to diffuse more effectively in qHP C_{60} . The PBEsol band gap of 0.86 eV is in line with previous calculations⁴². The HSEsol band gap of 1.44 eV is much narrower compared to the PBEsol0 gap of 2.12 eV, which can be attributed to an increase in the dielectric screening of HSEsol⁷¹.

To gain insight into the appropriate level of theory to correctly describe the electronic structures and optical properties of the C_{60} monolayers, the optical band gaps of monolayer fullerene networks are calculated and

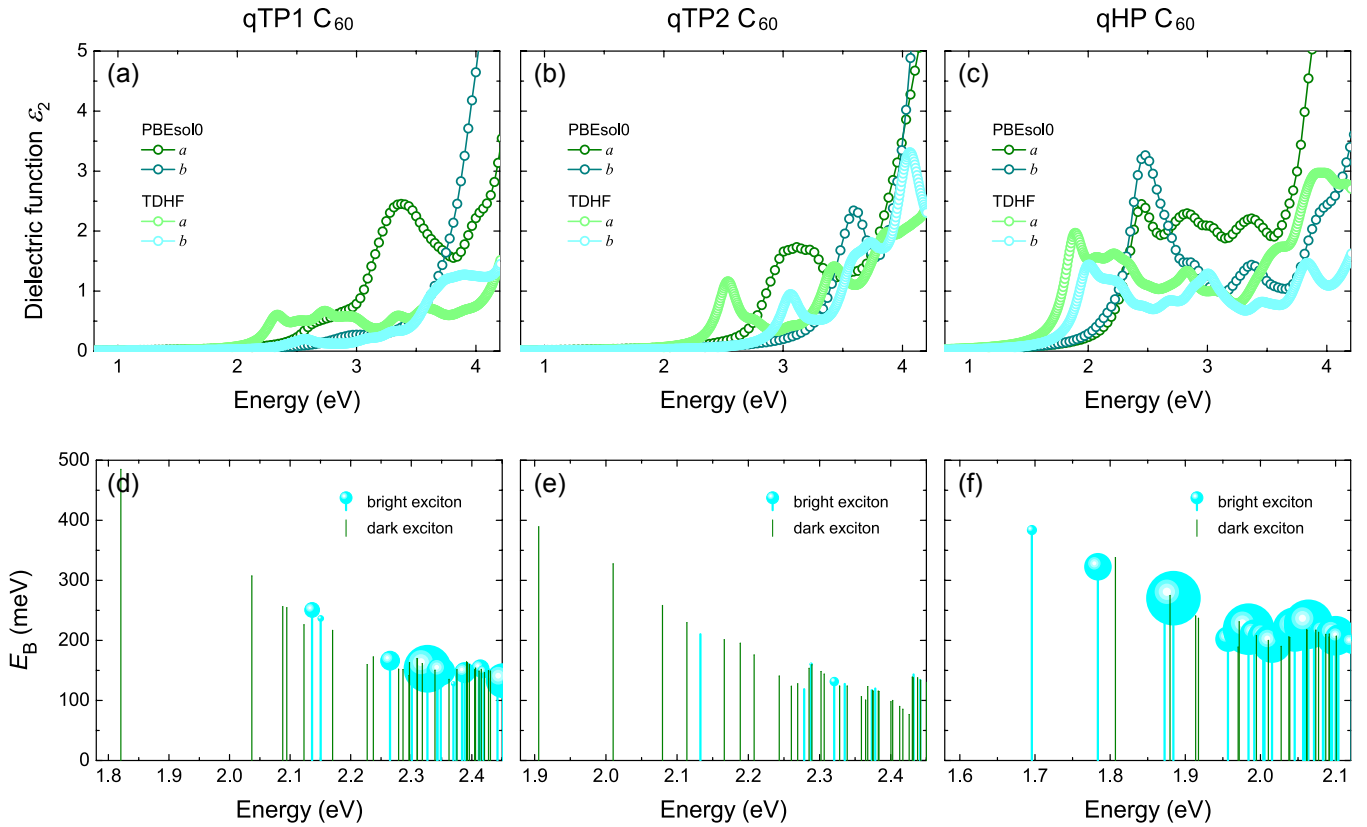


FIG. 3. Imaginary part of the dielectric function ϵ_2 of (a) qTP1, (b) qTP2, and (c) qHP C_{60} calculated with PBEsol0 and TDHF on top of PBEsol0, as well as the binding energy E_B of the low-energy excitons in (d)-(f). The radius of the bright excitons indicates the oscillator strength. The larger the radius, the higher the oscillator strength.

compared with the experimentally determined value. In 2D materials, the excitonic effects are stronger than their bulk counterparts due to weaker dielectric screening^{55,65,72}. To include exciton binding energy, time-dependent Hartree-Fock (TDHF) calculations are performed on top of PBEsol0 using a \mathbf{k} -mesh of 8×8 (5×8) with the highest eight (sixteen) valence bands and the lowest eight (sixteen) conduction bands included as basis for qTP (qHP) C_{60} , converging the exciton eigenenergy within 1 meV. In 2D materials, the exciton absorption spectrum calculated from TDHF agrees qualitatively well with the results obtained from the Bethe-Salpeter equation (BSE) on top of the GW calculations⁶⁵, and TDHF is computationally much less expensive than $GW + BSE$, especially for large systems such as monolayer fullerene networks. For qHP C_{60} , PBEsol0 + TDHF yields an optical band gap of 1.69 eV, in good agreement with the experimental value of 1.6 eV³⁸. The tiny discrepancy may come from temperature effects such as electron-phonon coupling⁷³⁻⁷⁷, which are not included in the calculations. On the other hand, the PBEsol and HSEsol band gaps, even without including the exciton binding energy, are lower than the measured gap. This is unsurprising because in quasi-0D C_{60} monolayers the screening effects are much weaker than most 2D materials, and consequently even the screened hybrid functional is inadequate

to describe the correct band gap. Thus a correct description of the band structures and optical properties can only be obtained by using TDHF on top of the unscreened hybrid functional PBEsol0.

The dielectric function of monolayer fullerene networks is first calculated by using PBEsol0, corresponding to the optical absorption of the hybrid-functional electronic structure under the independent particle picture. A nominal layer thickness of 14.78 Å and 16.94 Å are used for the dielectric function of qTP and qHP C_{60} respectively, corresponding to the interlayer distance of their bulk counterparts. The imaginary parts of the dielectric function of all three phases are gathered in Fig. 3(a)-(c). Within the independent particle approximation, the PBEsol0 dielectric function of both qTP1 and qTP2 C_{60} is strongly anisotropic along the a and b directions, whereas the first absorption peaks of qHP C_{60} have similar energies along both directions. Moreover, the indirect band gaps of qTP1 and qTP2 C_{60} give rise to low optical absorption in the visible light region.

Beyond the independent particle approximation, the dielectric function is evaluated by PBEsol0 + TDHF to assess the excitonic contributions, as demonstrated by the green and cyan curves in Fig. 3(a)-(c). In monolayer qTP1 C_{60} , including excitonic effects leads to a moderate sub-band-gap optical absorption, as shown in Fig. 3(a).

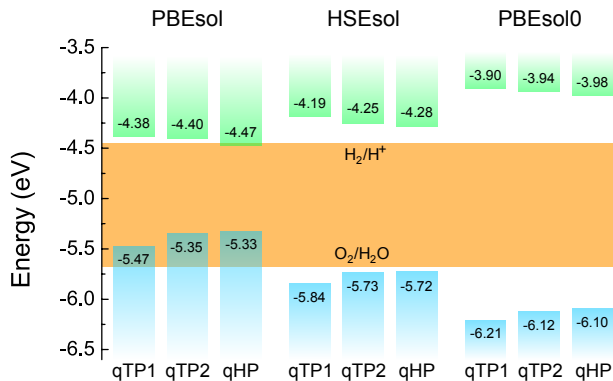


FIG. 4. Band alignment of qTP1, qTP2 and qHP C_{60} monolayers calculated with PBEsol, HSEsol and PBEsol0.

This is because the low-energy excitons are mostly dark and the optical transitions involved in these dark excitons have zero oscillator strength, as demonstrated in Fig. 3(d). Regarding the monolayer qTP2 C_{60} , the exciton absorption peak is even higher than the band gap of 2.18 eV owing to the zero oscillator strength in the optical transitions in the low-energy range. On the other hand, strong exciton absorption peak below the band gap is observed in monolayer qHP C_{60} in Fig. 3(c). The low-energy excitons in monolayer qHP C_{60} are mostly bright with large binding energy around 200 – 400 meV, as present in Fig. 3(f). Therefore, strong exciton absorption is induced in qHP C_{60} .

The PBEsol0 band gaps of the monolayer C_{60} networks around 2 eV can maximize the solar energy absorption for water splitting^{11,13}. For an overall water splitting reaction, the energy levels of the CBM and VBM must straddle the redox potentials of water. In other words, at pH = 0 the CBM (with respect to the vacuum level) should be higher than the hydrogen evolution potential of -4.44 eV, while the VBM should be lower than the oxygen evolution potential of -5.67 eV^{53,57,78}. To determine the band edge positions of qTP1, qTP2 and qHP C_{60} monolayers, the vacuum levels of all three phases are calculated by averaging the electrostatic potential along the c axis. Figure 4 summarizes the PBEsol0 band alignment of all three C_{60} monolayers, with the PBEsol and HSEsol band alignment plotted as well for comparison.

In monolayer qTP1 C_{60} , the PBEsol0 CBM is 0.54 eV higher than the reduction reaction potential of H_2/H^+ , which is suitable for water reduction. Moreover, the VBM is 0.54 eV lower than the oxidation potential of O_2/H_2O , which is suitable for water oxidation. Similarly, the CBM of qTP2 C_{60} is 0.50 eV higher than the reduction potential and the VBM is 0.45 eV lower than the oxidation potential. Regarding the monolayer qHP C_{60} , the CBM lies 0.46 eV above the reduction potential and the VBM is 0.43 eV below the oxidation potential. Therefore, all three C_{60} monolayers exhibit large band gaps with appropriate band edge positions for overall photocatalytic water splitting.

In addition, monolayer fullerene networks can be combined with a highly diverse set of lattice-matched 2D materials, such as AlN and WS_2 with higher CBM and VBM^{39–41,47}, to form type-II heterostructures to separate electrons and holes in individual layers, which can further improve the photocatalytic performance. The presence of monolayer fullerene networks can improve the separation of electrons and holes by trapping them individually into different nanostructures, i.e. 0D C_{60} cages in all three phases, or 1D C_{60} chains in qTP1 fullerene. For the 0D C_{60} cages in all three phases, the non-localized π bonds in C_{60} allows continuous transfer and separation of the photogenerated carriers²². For the 1D chains in qTP1 C_{60} , photogenerated carriers can move along the chain direction, and such 1D chain structures usually have a high carrier mobility^{13,16}. Furthermore, the enhanced surface area in monolayer fullerene networks, with more micropores and surface active sites compared to any 2D materials, can significantly increase the photocatalytic efficiency. Additionally, the optical transition oscillator strength in both the qTP1 and qTP2 monolayers is quite low, thereby suppresses the carrier recombination and enhances the photocatalytic efficiency as an electron acceptor. Regarding the monolayer qHP C_{60} , the strong optical absorption can generate a large amount of electrons, making it promising for providing electrons for hydrogen evolution.

The lattice parameters of 3×1 qTP1 C_{60} and 2×1 qHP C_{60} are matched within 3.8% for a and 0.8% for b respectively, therefore monolayer qTP1 and qHP C_{60} can also be combined to form qTP1/qHP heterostructures. To identify the type of the heterostructures for device applications, the band alignment at the qTP1/qHP interface is investigated. Compared to qTP1 C_{60} , qHP C_{60} has a consistently smaller band gap (see Table I and Fig. 4). The offset between the conduction band edges of qTP1 and qHP C_{60} monolayers is 0.08 eV with the CBM of qHP lower than that of qTP, and a higher VBM of qHP relative to qTP1 leads to a valence band discontinuity of 0.11 eV. Consequently, a type-I (straddling gap) band alignment exists between qTP1 and qHP C_{60} . The type-I heterostructures with qTP1 and qHP C_{60} can be utilized in optical devices such as light-emitting diodes owing to high emission efficiency⁷⁹, or in lasers because of efficient recombination of spatially confined electrons and holes in qHP C_{60} ³⁹.

In summary, I use unscreened hybrid functional and time-dependent Hartree-Fock calculations to examine the electronic structures and exciton binding energy of monolayer qTP and qHP C_{60} , rationalizing the measured optical band gap. To gain insights into the photocatalytic performance of monolayer fullerene networks, I investigate the band alignment of monolayer fullerene networks, and find that all three phases have the band edge positions suitable for overall water splitting. The distinct optical properties between qTP and qHP fullerene provide unique advantages for different applications in photocatalysis, with qTP C_{60} being a likely electron acceptor

and qHP C₆₀ being a promising electron donor respectively. Beyond water splitting, the type-I band alignment for the qTP1/qHP heterostructures offers new opportunities for optical devices and lasers.

ACKNOWLEDGMENTS

I thank Prof. Bartomeu Monserrat and Dr Ivona Bravić at the University of Cambridge for helpful dis-

cussions. I acknowledge support from the Winton Programme for the Physics of Sustainability. The calculations were performed using resources provided by the Cambridge Tier-2 system, operated by the University of Cambridge Research Computing Service (www.hpc.cam.ac.uk) and funded by EPSRC Tier-2 capital grant EP/P020259/1, as well as with computational support from the U.K. Materials and Molecular Modelling Hub, which is partially funded by EPSRC (EP/P020194), for which access is obtained via the UKCP consortium and funded by EPSRC grant ref. EP/P022561/1.

-
- * bp432@cam.ac.uk
- ¹ P. Bhatia, S. Burch, J. Emmet-Booth, J. S. Fuglestedt, M. Kelller, J. Kikstra, M. König, M. Meinhäuser, Z. Nicholls, and K.-I. van der Wijst, in [Climate Change 2022: Mitigation of Climate Change](#), Contribution of Working Group III to the Sixth Assessment Report of the Intergovernmental Panel on Climate Change, edited by P. Shukla, J. Skea, R. Slade, A. A. Khoualdjia, R. van Diemen, D. McCollum, M. Pathak, S. Some, P. Vyas, R. Fradera, M. Belkacemi, A. Hasija, G. Lisboa, S. Luz, and J. Malley (Cambridge University Press, Cambridge, UK, 2022).
 - ² A. Fujishima and K. Honda, [Nature](#) **238**, 37 (1972).
 - ³ P. Deák, B. Aradi, and T. Frauenheim, [J. Phys. Chem. C](#) **115**, 3443 (2011).
 - ⁴ D. O. Scanlon, C. W. Dunnill, J. Buckeridge, S. A. Shevlin, A. J. Logsdail, S. M. Woodley, C. R. A. Catlow, M. J. Powell, R. G. Palgrave, I. P. Parkin, G. W. Watson, T. W. Keal, P. Sherwood, A. Walsh, and A. A. Sokol, [Nature Materials](#) **12**, 798 (2013).
 - ⁵ V. Pfeifer, P. Erhart, S. Li, K. Rachut, J. Morasch, J. Brötz, P. Reckers, T. Mayer, S. Rühle, A. Zaban, I. Mora Seró, J. Bisquert, W. Jaegermann, and A. Klein, [J. Phys. Chem. Lett.](#) **4**, 4182 (2013).
 - ⁶ M.-G. Ju, G. Sun, J. Wang, Q. Meng, and W. Liang, [ACS Appl. Mater. Interfaces](#) **6**, 12885 (2014).
 - ⁷ Y. Mi and Y. Weng, [Sci. Rep.](#) **5**, 11482 (2015).
 - ⁸ D. Zhang, M. Yang, and S. Dong, [Phys. Chem. Chem. Phys.](#) **17**, 29079 (2015).
 - ⁹ P. Deák, J. Kullgren, B. Aradi, T. Frauenheim, and L. Kavan, [Electrochimica Acta](#) **199**, 27 (2016).
 - ¹⁰ L. Chiodo, J. M. García-Lastra, A. Iacomino, S. Ossicini, J. Zhao, H. Petek, and A. Rubio, [Phys. Rev. B](#) **82**, 045207 (2010).
 - ¹¹ T. Le Bahers, M. Rérat, and P. Sautet, [J. Phys. Chem. C](#) **118**, 5997 (2014).
 - ¹² Z. Wang, C. Li, and K. Domen, [Chem. Soc. Rev.](#) **48**, 2109 (2019).
 - ¹³ K. Brlec, S. R. Kavanagh, C. N. Savory, and D. O. Scanlon, [ACS Appl. Energy Mater.](#) **5**, 1992 (2022).
 - ¹⁴ L. Zhang, W. Wang, L. Zhou, and H. Xu, [Small](#) **3**, 1618 (2007).
 - ¹⁵ Y. Zhang, J. Yu, D. Yu, X. Zhou, and W. Lu, [Rare Metals](#) **30**, 192 (2011).
 - ¹⁶ T. Suzuki, T. Hisatomi, K. Teramura, Y. Shimodaira, H. Kobayashi, and K. Domen, [Phys. Chem. Chem. Phys.](#) **14**, 15475 (2012).
 - ¹⁷ H.-Y. Jiang, J. Liu, K. Cheng, W. Sun, and J. Lin, [J. Phys. Chem. C](#) **117**, 20029 (2013).
 - ¹⁸ J. Xu, L. Li, C. Guo, Y. Zhang, and W. Meng, [Applied Catalysis B: Environmental](#) **130-131**, 285 (2013).
 - ¹⁹ J. Zhu, Z. Yin, D. Yang, T. Sun, H. Yu, H. E. Hoster, H. H. Hng, H. Zhang, and Q. Yan, [Energy Environ. Sci.](#) **6**, 987 (2013).
 - ²⁰ A. Nakada, D. Kato, R. Nelson, H. Takahira, M. Yabuuchi, M. Higashi, H. Suzuki, M. Kirsanova, N. Kakudou, C. Tassel, T. Yamamoto, C. M. Brown, R. Dronskowski, A. Saeki, A. Abakumov, H. Kageyama, and R. Abe, [J. Am. Chem. Soc.](#) **143**, 2491 (2021).
 - ²¹ D. Luo, K. Yin, and R. Dronskowski, [J. Am. Chem. Soc.](#) **144**, 5155 (2022).
 - ²² Y. Pan, X. Liu, W. Zhang, Z. Liu, G. Zeng, B. Shao, Q. Liang, Q. He, X. Yuan, D. Huang, and M. Chen, [Applied Catalysis B: Environmental](#) **265**, 118579 (2020).
 - ²³ S. Yao, X. Yuan, L. Jiang, T. Xiong, and J. Zhang, [Materials](#) **13**, 2924 (2020).
 - ²⁴ H. W. Kroto, J. R. Heath, S. C. O'Brien, R. F. Curl, and R. E. Smalley, [Nature](#) **318**, 162 (1985).
 - ²⁵ E. M. Barker and J. P. Buchanan, [Polymer](#) **92**, 66 (2016).
 - ²⁶ Q. Chen, M.-Q. Cheng, K. Yang, W.-Q. Huang, W. Hu, and G.-F. Huang, [J. Phys. D: Appl. Phys.](#) **51**, 305301 (2018).
 - ²⁷ D. Ma, J. Zhong, R. Peng, J. Li, and R. Duan, [Applied Surface Science](#) **465**, 249 (2019).
 - ²⁸ V. Arivazhagan, J. Xie, P. Hang, M. Manonmani Parvathi, A. Khan, C. Cui, D. Yang, and X. Yu, [J. Phys. D: Appl. Phys.](#) **52**, 225104 (2019).
 - ²⁹ P. V. Kamat, I. Bedja, and S. Hotchandani, [J. Phys. Chem.](#) **98**, 9137 (1994).
 - ³⁰ J. Yu, T. Ma, G. Liu, and B. Cheng, [Dalton Trans.](#) **40**, 6635 (2011).
 - ³¹ Z. Youssef, L. Colombeau, N. Yesmurzayeva, F. Baros, R. Vanderesse, T. Hamieh, J. Toufaily, C. Frochet, T. Roques-Carmes, and S. Acherar, [Dyes and Pigments](#) **159**, 49 (2018).
 - ³² G. D. Panagiotou, M. D. Tzirakis, J. Vakros, L. Loukatzikou, M. Orfanopoulos, C. Kordulis, and A. Lycourghiotis, [Applied Catalysis A: General](#) **372**, 16 (2010).
 - ³³ T. Song, J. Huo, T. Liao, J. Zeng, J. Qin, and H. Zeng, [Chemical Engineering Journal](#) **287**, 359 (2016).
 - ³⁴ H. Fu, T. Xu, S. Zhu, and Y. Zhu, [Environ. Sci. Technol.](#)

- 42**, 8064 (2008).
- ³⁵ Z. Du, W. Li, Z. Xu, H. Wu, H. Jameel, H.-M. Chang, and L.-L. Ma, *Journal of Wood Chemistry and Technology* **36**, 365 (2016).
- ³⁶ Q. Wang and P. Jena, *J. Phys. Chem. Lett.* **3**, 1084 (2012).
- ³⁷ D. Durbin, N. Allan, and C. Malardier-Jugroot, *International Journal of Hydrogen Energy* **41**, 13116 (2016).
- ³⁸ L. Hou, X. Cui, B. Guan, S. Wang, R. Li, Y. Liu, D. Zhu, and J. Zheng, *Nature* **606**, 507 (2022).
- ³⁹ V. O. Özçelik, J. G. Azadani, C. Yang, S. J. Koester, and T. Low, *Phys. Rev. B* **94**, 035125 (2016).
- ⁴⁰ W. Hu and J. Yang, *J. Mater. Chem. C* **5**, 12289 (2017).
- ⁴¹ X. Yang, D. Singh, and R. Ahuja, *Catalysts* **10**, 1111 (2020).
- ⁴² R. M. Tromera, L. A. R. Juniorc, and D. S. Galvãoa, arXiv:2207.01663 (2022).
- ⁴³ L. Yu, J. Xu, B. Peng, G. Qin, and G. Su, arXiv:2207.02781 (2022).
- ⁴⁴ B. Peng, H. Zhang, H. Shao, Z. Ning, Y. Xu, G. Ni, H. Lu, D. W. Zhang, and H. Zhu, *Materials Research Letters* **5**, 399 (2017).
- ⁴⁵ J. Guan, J. Wu, D. Jiang, X. Zhu, R. Guan, X. Lei, P. Du, H. Zeng, and S. Yang, *International Journal of Hydrogen Energy* **43**, 8698 (2018).
- ⁴⁶ K. Kim, S. Larentis, B. Fallahazad, K. Lee, J. Xue, D. C. Dillen, C. M. Corbet, and E. Tutuc, *ACS Nano* **9**, 4527 (2015).
- ⁴⁷ C. Zhang, C. Gong, Y. Nie, K.-A. Min, C. Liang, Y. J. Oh, H. Zhang, W. Wang, S. Hong, L. Colombo, R. M. Wallace, and K. Cho, *2D Materials* **4**, 015026 (2016).
- ⁴⁸ Z. G. Yu, Y.-W. Zhang, and B. I. Yakobson, *J. Phys. Chem. C* **120**, 22702 (2016).
- ⁴⁹ D. Pierucci, H. Henck, J. Avila, A. Balan, C. H. Naylor, G. Patriarache, Y. J. Dappe, M. G. Silly, F. Sirotti, A. T. C. Johnson, M. C. Asensio, and A. Ouerghi, *Nano Lett.* **16**, 4054 (2016).
- ⁵⁰ H. M. Hill, A. F. Rigosi, K. T. Rim, G. W. Flynn, and T. F. Heinz, *Nano Lett.* **16**, 4831 (2016).
- ⁵¹ Z. Zhang, Q. Qian, B. Li, and K. J. Chen, *ACS Appl. Mater. Interfaces* **10**, 17419 (2018).
- ⁵² R. Zhang, L. Zhang, Q. Zheng, P. Gao, J. Zhao, and J. Yang, *J. Phys. Chem. Lett.* **9**, 5419 (2018).
- ⁵³ X. Zhang, A. Chen, Z. Zhang, M. Jiao, and Z. Zhou, *Nanoscale Adv.* **1**, 154 (2019).
- ⁵⁴ C.-F. Fu, C. Zhao, Q. Zheng, X. Li, J. Zhao, and J. Yang, *Science China Chemistry* **63**, 1134 (2020).
- ⁵⁵ R. Zhang, X. Wen, F. Xu, Q. Zhang, and L. Sun, *J. Phys. Chem. C* **124**, 11922 (2020).
- ⁵⁶ S. Han, Y. Li, and Z. Wang, *Phys. Chem. Chem. Phys.* **22**, 17145 (2020).
- ⁵⁷ H. Chen, J. Zhao, X. Wang, X. Chen, Z. Zhang, and M. Hua, *Nanoscale* **14**, 5551 (2022).
- ⁵⁸ D. Yuan, H. Pi, Y. Jiang, Y. H. L. Zhou, Y. Jia, G. Su, Z. Fang, H. Weng, X. Ren, and W. Zhang, arXiv:2207.11366 (2022).
- ⁵⁹ J. P. Perdew, A. Ruzsinszky, G. I. Csonka, O. A. Vydrov, G. E. Scuseria, L. A. Constantin, X. Zhou, and K. Burke, *Phys. Rev. Lett.* **100**, 136406 (2008).
- ⁶⁰ G. Kresse and J. Furthmüller, *Phys. Rev. B* **54**, 11169 (1996).
- ⁶¹ G. Kresse and J. Furthmüller, *Computational Materials Science* **6**, 15 (1996).
- ⁶² S. Grimme, J. Antony, S. Ehrlich, and H. Krieg, *J. Chem. Phys.* **132**, 154104 (2010).
- ⁶³ K. Momma and F. Izumi, *Journal of Applied Crystallography* **44**, 1272 (2011).
- ⁶⁴ L. Schimka, J. Harl, and G. Kresse, *J. Chem. Phys.* **134**, 024116 (2011).
- ⁶⁵ B. Peng, H. Zhang, H. Shao, K. Xu, G. Ni, L. Wu, J. Li, H. Lu, Q. Jin, and H. Zhu, *ACS Photonics* **5**, 4081 (2018).
- ⁶⁶ Z. Li, B. Peng, M.-L. Lin, Y.-C. Leng, B. Zhang, C. Pang, P.-H. Tan, B. Monserrat, and F. Chen, *npj 2D Materials and Applications* **5**, 87 (2021).
- ⁶⁷ G. Su, A. Gao, B. Peng, J. Hu, Y. Zhang, F. Liu, H. Zhang, P. Zhan, and W. Wu, *Nanophotonics* **11**, 3149 (2022).
- ⁶⁸ J. P. Perdew, M. Ernzerhof, and K. Burke, *J. Chem. Phys.* **105**, 9982 (1996).
- ⁶⁹ C. Adamo and V. Barone, *J. Chem. Phys.* **110**, 6158 (1999).
- ⁷⁰ M. Ernzerhof and G. E. Scuseria, *J. Chem. Phys.* **110**, 5029 (1999).
- ⁷¹ C. N. Savory, R. G. Palgrave, H. Bronstein, and D. O. Scanlon, *Sci. Rep.* **6**, 20626 (2016).
- ⁷² S. Latini, K. T. Winther, T. Olsen, and K. S. Thygesen, *Nano Lett.* **17**, 938 (2017).
- ⁷³ W. A. Saidi, S. Poncé, and B. Monserrat, *J. Phys. Chem. Lett.* **7**, 5247 (2016).
- ⁷⁴ B. Monserrat, J.-S. Park, S. Kim, and A. Walsh, *Appl. Phys. Lett.* **112**, 193903 (2018).
- ⁷⁵ Y.-N. Wu, W. A. Saidi, P. Ohodnicki, B. Chorpene, and Y. Duan, *J. Phys. Chem. C* **122**, 22642 (2018).
- ⁷⁶ B. Peng, I. Bravić, J. L. MacManus-Driscoll, and B. Monserrat, *Phys. Rev. B* **100**, 161101 (2019).
- ⁷⁷ A. Miglio, V. Brousseau-Couture, E. Godbout, G. Antonius, Y.-H. Chan, S. G. Louie, M. Côté, M. Giantomassi, and X. Gonze, *npj Computational Materials* **6**, 167 (2020).
- ⁷⁸ V. Chakrapani, J. C. Angus, A. B. Anderson, S. D. Wolter, B. R. Stoner, and G. U. Sumanasekera, *Science* **318**, 1424 (2007).
- ⁷⁹ B. Zheng, C. Ma, D. Li, J. Lan, Z. Zhang, X. Sun, W. Zheng, T. Yang, C. Zhu, G. Ouyang, G. Xu, X. Zhu, X. Wang, and A. Pan, *J. Am. Chem. Soc.* **140**, 11193 (2018).